Fabrication control of MoS2/MoO2 nanocomposite via chemical vapor deposition for optoelectronic applications

D. Mouloua, N.S. Rajput, Jean-François Blach, M. Lejeune, M. El Marssi, M.A. El Khakani, M. Jouiad

Fabrication control of MoS_2/MoO_2 nanocomposite via chemical vapor deposition for optoelectronic applications

D. Mouloua[1,2], NS. Rajput[3], J-F. Blach[4], M. Lejeune[1], M. El Marssi[1], M. A. El Khakani[2,*], M. Jouiad[1,*]

[1]*Laboratory of Physics of Condensed Matter, University of Picardie Jules Verne, Scientific Pole, 33 rue Saint-Leu, 80039 Amiens Cedex 1, France*
[2]*Institut National de la Recherche Scientifique (INRS), Centre-Énergie, Matériaux et Télécommunications, 1650, Blvd, Lionel–Boulet, Varennes, QC J3X-1S2, Canada*
[3]*Advanced Materials Research Center, Technology Innovation Institute, P.O. Box 9639, Abu Dhabi, United Arab Emirates*
[4]*Univ. Artois, CNRS, Centrale Lille, ENSCL, Univ. Lille, UMR 8181, Unité de Catalyse et Chimie du Solide (UCCS), F-62300 Lens, France*
[*]Corresponding authors: m.a.elkhakani@inrs.ca; mustapha.jouiad@u-picardie.fr

Abstract

We report on the fabrication and control of MoS_2/MoO_2 nanocomposites exhibiting various optoelectronic properties. We demonstrate the growth of various compositions, shapes and crystalline structures by chemical vapor deposition (CVD). Microplates 1 to 30 µm to highly crystalline nanowires ~100 nm in diam. are obtained. Our findings show that depending on the MoO_2 content the band gap varies from 2 eV to 2.4 eV, whereas nanowires sample exhibits the lowest reflectance ≤ 10% for λ ≥ 450 nm. Furthermore, the photoelectric properties of the produced samples were characterized by integrating them into photoconductive devices. Our results demonstrate a good photoresponse achieving 2 x 10^4 %, a responsivity as high as 1.13 mA/W, and a specific detectivity of 2.6 x 10^9 Jones for the nanowires, with a relatively rapid rise and decay times 1.6 s and 0.8 s, respectively. This work emphasizes the high potential of MoS2/MoO2 nanocomposite for the development of highly responsive optoelectronic devices.

Keywords: MoS_2/MoO_2 nanocomposite, MoS_2/MoO_2 heterostructure, MoS_2 nanowires, chemical vapor deposition, photocurrent, photoresponse.

1. Introduction

Over the past decade, molybdenum disulfide (MoS_2) has increasingly attracted attention due to its outstanding electrical and optical properties[1–4]. MoS_2 is a layered semiconductor that is sought to be used in optoelectronic devices with high on-off current ratios [5], owing to its tunable band gap [6,7] and its high electronic mobility [8]. When MoS_2 is associated with other materials, the resulting heterostructures could lead to a wide range of applications [9–15].

MoS_2-based photodetectors have been widely reported in the literature. Notably, engineering MoS_2-based heterostructures is among the most investigated strategies for the improvement of the photodetection performances [16]. Their main advantage consists in their ability to enable high charge carrier nucleation and transport and fast photodetection response by generating built-in electric fields [17]. Although a large variety of materials have been coherently associated with MoS_2, their elaboration remains relatively tedious, generally requiring a two steps fabrication process, hence raising the overall costs of the photodetector devices [18–20]. In this sense, the chemical vapor deposition (CVD) approach prevails as the most accessible, affordable and straightforward route for producing good-crystalline quality MoS_2[21–23]. Nonetheless, the CVD growth of MoS_2 is sensitive to various parameters, including ambient pressure, carrier gas flow, furnace temperature, CVD reaction dwell time, precursor's positions, substrate location, etc. Evaluating each parameter is critical to obtain high-quality crystalline, mono to few MoS_2 layers with controlled morphologies and properties [24–28]. A comprehensive review regarding the MoS_2 growth via CVD, including growth parameters effects can be found elsewhere[29,30].

Although the CVD method allows the fabrication of highly crystalline MoS_2 films with a variety of morphologies, one of its limit is the loss of purity of MoS_2 due to incomplete sulfidation of metal precursors [31]. In other words, several intermediate materials, such as MoO_3[32], MoO_2[33], $MoOS_2$[34] would have been synthesized as already investigated[35] . Recently, other researchers have pointed out the possible beneficial effects of hybridizing such intermediate materials with MoS_2 to improve the overall optical performance of the final hybrid materials[36]. Nonetheless, the control of the MoS_2/MoO_2 phase ratio throughout the CVD process and its effect on the properties of the resulting nanocomposite has not been investigated yet.

In this work, we report a systematic investigation of the MoS_2/MoO_2 nanocomposites where the MoS_2/MoO_2 phase ratio can be controlled through the tuning of the CVD key parameters. Thus, various variants of the MoS_2/MoO_2 nanocomposite with engineered band gaps were achieved and used to for the photodetection.

2. Materials and Methods

2.1. CVD growth

Molybdenum trioxide (MoO_3, 99.99%) and sulfur (S, 99.5%) were used to synthesize high crystalline planar and vertical MoS_2 and MoO_2 crystals on silicon (Si) substrates using a CVD system. A ceramic boat with 250 mg of sulfur (S) was placed upstream was placed upstream in a low-temperature zone 27.5 cm from the flow inlet. Eight substrates were cleaned by acetone and ethanol, rinsed by deionized-water and dried out using nitrogen gas flow prior to their introduction in the furnace. The substrates were placed in the high- temperature zone and 30 mg of MoO_3 and 5 mg of S were added on the substrate located at position #0 on samples holder which is placed 50 cm from the tube inlet (**Figure 1**a). Four other substrates were placed after sample #0 in the same flow direction, positions #1 to #4, and three substrates are placed before sample #0 in the opposite direction of flow, positions # -1 to # -3 (**Figure 1**a). **Figure 1**b shows the temperature variation in the furnace as a function of time. The center of the furnace was heated from room temperature to 400°C at a heating rate of 20°C/min. This rate was selected to achieve a rapid sulfur evaporation and avoid a complete reaction of of MoO_3 powder favoring

thereby the formation of a hybrid material containing MoS_2 and MoO_2. Then, a second heating rate of 10°C/min was applied up to 600°C, this heating segment is intended to slowdown the evaporation of MoO_3. Finally, a third heating rate of 6°C/min was applied to attain the processing temperature of 850°C maintained for a total reaction dwell time of 30 min (**Figure 1**c). All the syntheses were carried out at atmospheric pressure using ultra-high purity gas carrier Argon (99.998 %) at 70 sccm flow rate during the whole CVD process. Finally, the furnace was shut down and the samples were cooled down naturally to room temperature while keeping the gas flow.

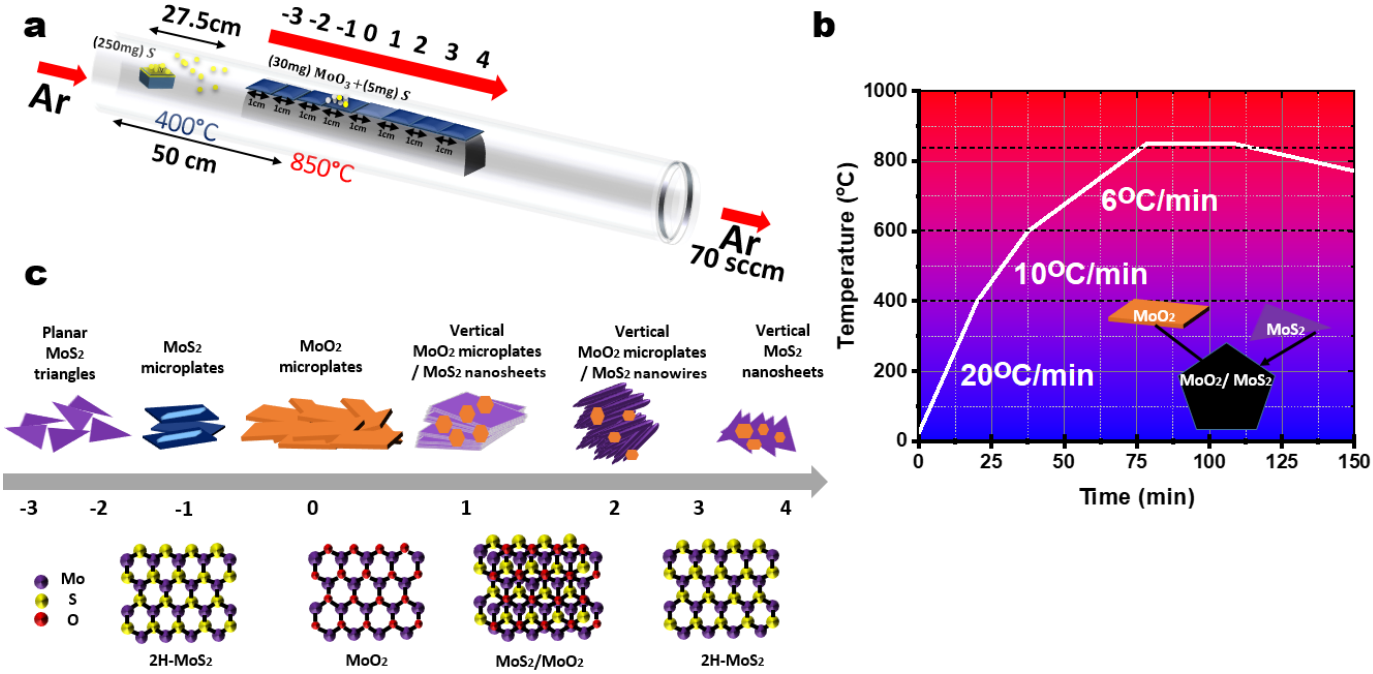

Figure 1. a. Fabrication workflow of MoS_2/MoO_2 nanocomposite by CVD process using quartz tube, **b.** heating rate profile of different heating segments, **c.** representation of the typical MoS_2/MoO_2 morphologies and chemical compositions as a function of the sample position in the furnace.

2.2. Material Characterization

The as-grown MoS_2/MoO_2 composites were first examined by optical microscopy using Olympus™ BX51M optical microscope in polarized mode. Then their microstructure was examined by scanning electron microscopy (SEM) Quanta 200 FEG, ThermofisherScientific™ and the chemical composition was determined through elemental mapping of the constituting elements using energy dispersive X-ray

spectroscopy (EDX) oxford instruments™. A dual focused ion beam system Helios ThermofisherScientific™ was used to prepare cross-sectional samples and thin lamella for transmission electron microscopy (TEM) investigations. Lamellas were prepared using a standard FIB lift-out technique. TEM analyses of the samples were conducted using an image Cs-corrected TEM system Titan Thermofisher Scientific™ operating at 300 kV. The vibrational modes of the processed samples were used to track the characteristic spectra associated with the various MoS_2 phases, using a micro-Raman spectrometer, Renishaw™, with a laser excitation of 532 nm. The crystalline structure was characterized by means of x-ray diffraction (XRD) using a D8 Discover diffractometry Bruker™ ($K_{\alpha Cu}$ = 1.54 Å). The optical properties were systematically investigated by means of UV-Vis-near IR spectrometer JASCO™ V-670. The spectroscopic ellipsometry was also employed, at room temperature, to complete the optical characterizations by using a phase-modulated ellipsometer UVISEL HR460 from Horiba Scientific™ covering the 300 – 1500 nm wavelength range with a 2 nm step interval and an incidence angle of 70°. Finally, electrical measurements were performed using Palmsens-4 electrochemical workstation under ambient conditions.

3. Results and discussion

3.1 Optical microscopy and Raman spectroscopy

Figure 2a shows snapshots of our samples' tray after the fabrication process. The samples #1 to #4 have a blueish color while the samples #-1 to # -3 are greyer. This indicates that the density/thickness of the films is not evenly distributed along the tube furnace length and it is a sample position dependent. As can be seen, samples #1 and #2 are the bluest ones, suggesting a higher thickness or the existence of specific morphology and/or chemical composition. **Figure 2**b displays the optical images of all samples. One can notice that the sample at the position #-3 contains planar MoS_2 micro-triangles with low density highlighted by dark arrows on the image. It is important to stress here that this morphology is the most common structure cited in the literature [30,37,38] . By comparing the images of **Figure 2**b**,** a morphology transformation from sample #-3 to sample #-1 can be

witnessed, namely from planar micro-triangles to planar microplates MoS_2 (with blue color, likely because of their higher thickness). The sample #0 contains a higher surface density of larger MoO_2 microplates (with red color) as confirmed by Raman spectroscopy shown in **Figure 2**c. As the sample position is changed from sample #1 to sample #4, the optical image color changes progressively from yellow-orange-brownish to an increasingly darker tone. As demonstrated using Raman spectroscopy provided in **Figure 2**c, this indicates the presence of MoO_2 which is vanishing towards the sample #4 where only MoS_2 is obtained. Indeed the Raman spectra show the Raman fingerprint of pure hexagonal structure of 2H-MoS_2 A_{1g} and E^1_{2g} modes [39]. In contrast, the MoO_2 spectra are intense and visible for sample #0 indicating the characteristic peaks of monoclinic (m) MoO_2 but they are missing for the sample #4.

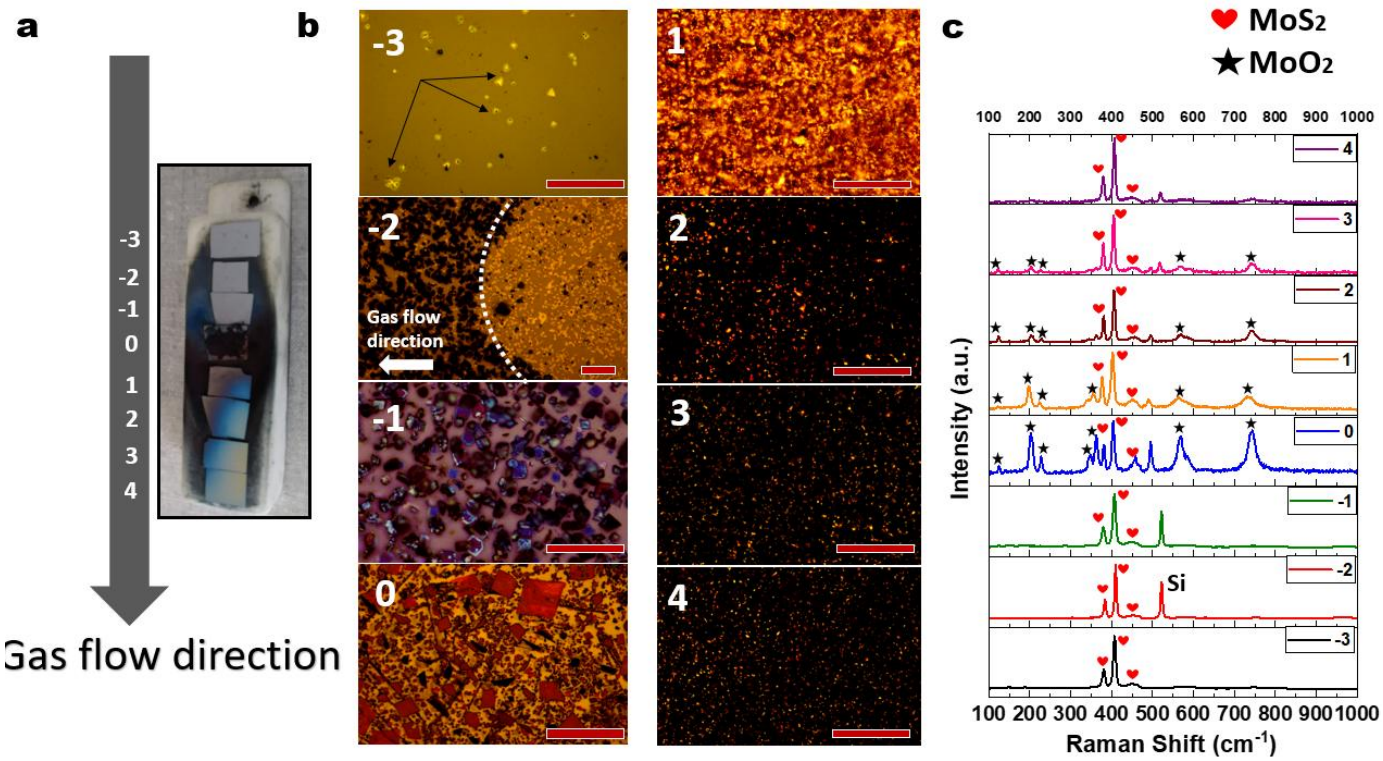

Figure 2. a. A snapshot of the processed samples as collected from the tube furnace **b.** typical optical images of the MoS_2/MoO_2 (scale bar 50 µm) samples at the eight different positions in the furnace; **c.** corresponding Raman spectra of the as a function of the sample positions.

3.2. XRD analysis and XPS spectroscopy

To confirm the structural and chemical transformation of the MoS_2/MoO_2 samples as a function of their position in the furnace, we have performed XRD analysis. **Figure 3**a shows the obtained XRD diagram, where the Miller

indices of diffracted planes are marked in black and in red for the phase 2H-MoS_2 (COD-96-101-0994) and m-MoO_2 (COD- 96-154-8688), respectively. The sample #-3 exhibits a weak reflection peak corresponding to (002) plans of 2H- MoS_2 and no extra peak is recoded, this result corroborates the Raman spectra obtained for this sample showingthe sole formation of MoS_2. As we move towards position of sample #-2, we notice the appearance of the (006) planes reflection of 2H-MoS_2 along with two peaks attributed to (200) and (031) family plans of m-MoO_2 (extra peaks belong to Si substrate). The m-MoO_2 associated peaks appear also for the samples #-1, #0, #1 and #2. For instance, (100) peak appeared for sample #-1 and (20-2), (21-1), (300), (-213), (22-2), and (211) peaks also appeared for sample #0 even if the only defined and intense one is the (21-1) peak (see the zoomed XRD region in **Figure 3**b). On the other hand, **Figure 3**a shows a progressive vanishing of the 2H-MoS_2 (200) peak intensity when sample position is changing from sample #-2 to sample #1. This suggests an increase in the amount of MoO_2 at the expense of MoS_2 phase in the direction from sample #-2 to sample #1. It can also be seen that sample #0 shows most of the MoO_2 XRD peaks. Finally, for samples #1, #2, #3 and #4, we noticed the recurrence of the (100) peak of MoS_2 and the progressive disappearance of the MoO_2 associated peaks, confirming the above-discussed results where the formation of the MoO_2 phase is favored around position #0 and the predominance of the MoS_2 phase increases as the position is changed towards the sample #4. The unmarked high peak at around $2\theta = 69^{o}$ and 45° correspondto the Si substrate, and the other unmarked peaks could be identified properly and are considered to be potentially due to impurities.

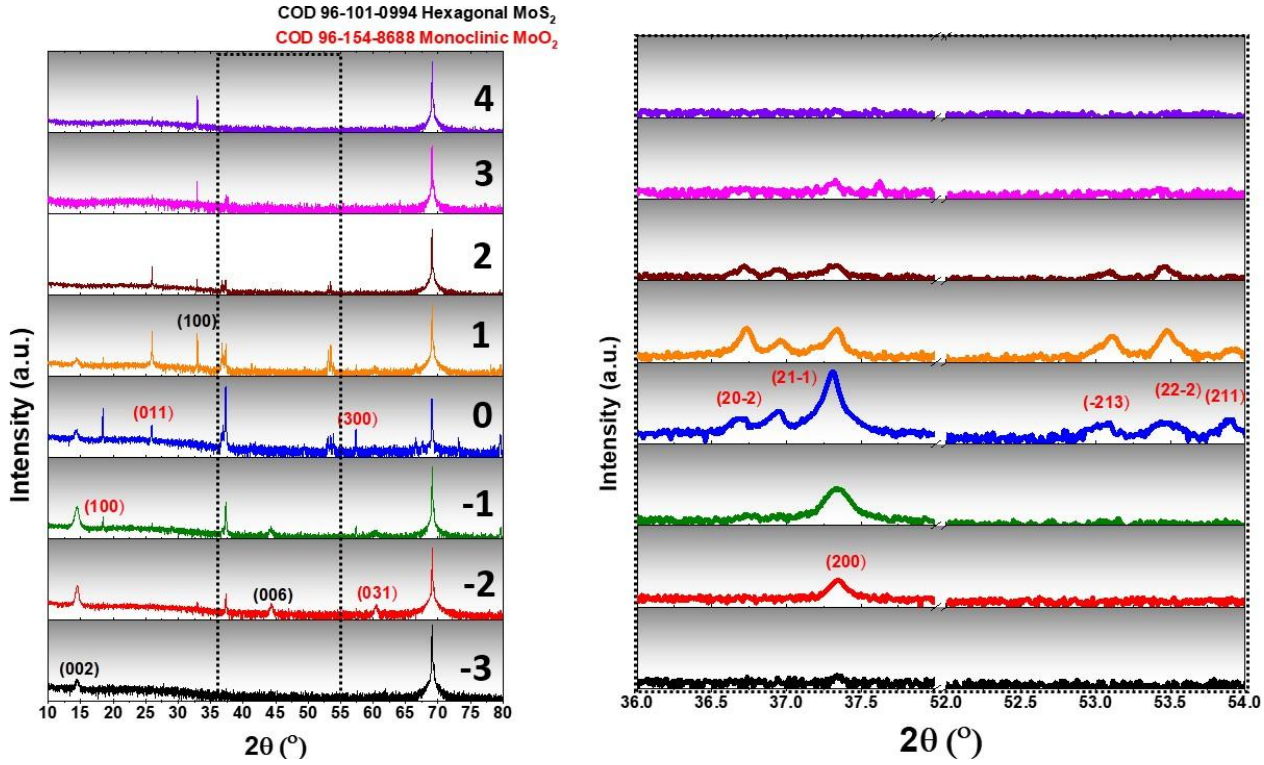

Figure 3. **a.** Typical XRD diagrams of our CVD grown MoS_2/MoO_2 nanocomposites; **b.** a zoomed view of the (36-54)° 2θ range.

Figure 4a shows the XPS survey of the sample #-3. Note that the XPS investigations were carried out in PHI VersaProbe II scanning XPS microprobe. The system used 15KV electron gun to produce monochromatic and microfocused Al K-alpha X-ray source of 1486.6 eV. All the obtained XPS spectra were calibrated using C1s as reference at 284.6 eV. The background was removed and subsequently the peaks were fitted with Gaussian functions.

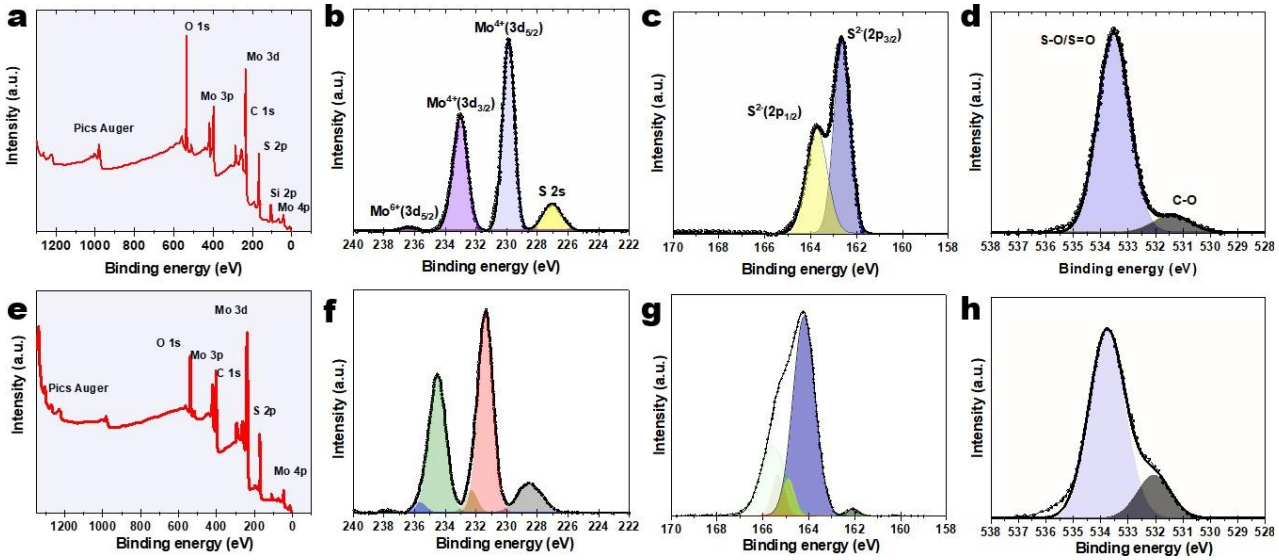

Figure 4. a. Typical XPS survey of sample #-3 and corresponding high-resolution XPS spectra of Mo 3d (**b.**), S 2s (**c.),** and O 1s (**e.**) core levels **e.** XPS survey of the sample #0 with its associated high-resolution Mo 3d (**f.**), S 2s (**g.)** S 2p and O 1s (**h.**) core levels.

The high-resolution XPS spectra of the Mo 3d, S 2s and O 1s core levels are displayed in **Figure 4**b-**4**d. In **Figure 4**b, the S 2s core level peak is observed at 227.2 eV in addition to the two peaks at 229.8 and 233.3 eV, which are attributed to the Mo $3d_{5/2}$ and Mo $3d_{3/2}$ doublet, respectively, corresponding to the Mo^{4+} states in MoS_2[40]. The small Mo 3d core level peak at 236.4 eV is attributed to the Mo^{6+} state of MoO_3[35]. Similarly, the S 2p spectra show the S^{2-} doublet of MoS_2 at 162.3 and 163.7 eV (**Figure 4**c)[41]. The binding energies of O 1s (**Figure 4**d) are due to S–O/S=O bonding states at 533.5 eV and to C–O bonding states at 531.5 eV [42]. On the other hand, **Figure 4**e shows the XPS survey of the sample #0, the **Figure 4**f shows the high-resolution XPS prominent peak located at 231.4 eV is due to Mo^{4+} bonding states in MoS_2 while the small peak centered around 232.3 eV is associated with of MoO_2[43]. The peak around 234.5 eV represents the $3d_{5/2}$ of Mo^{+10} (MoO_5) which is consistent with a higher ratio of MoO_2 in the sample#0 [37]. The deconvolution of the S 2p core level spectrum (**Figure 4**g) suggests that the peak at 162.3 eV is due to MoS_X with $x < 2$ [44], the peak at 163.7 eV is attributed to S $2p_{3/2}$, while the peak at 164.9 is attributed to S $2p_{1/2}$ in MoS_2/MoO_2 [43]. Correspondingly, the prominent component of the O1s peak located around 533.7 eV (see **Figure 4**h) is likely to be due to S–O/S=O bonding states in $MoOS_2$ [45], while the smaller component centered around 532.3 eV is due to C–O bonding states [46], originating from the unavoidable carbon contamination of the sample surface.

3.3. Microstructure analysis

An interesting aspect of our fabrication method is the possibility to influence the morphology of our samples. Both the simple's position in the furnace and its distance with respect to the precursors are the main parameters determining the composition and crystalline structure of the grown material. **Figure 5** shows the EDX mapping of sample #0 where the planar MoS_2/MoO_2 microplates with a size in the 10-100 µm range are clearly seen. The maps built on Mo, S, and O elements are clearly seen to reproduce the shapes of the MoS_2/MoO_2 microplates.

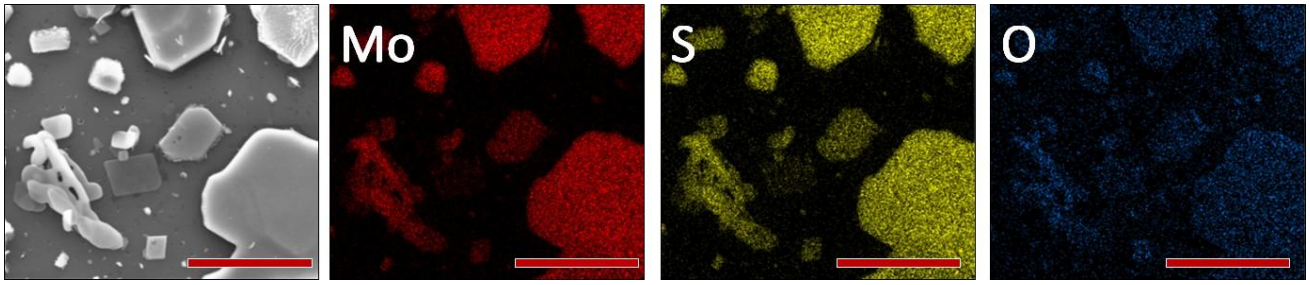

Figure 5. Typical EDX elemental chemical maps of Mo, S and O elements recorded in the sample 0 (scale bar 100 µm).

Figure 6 compares the SEM images of the CVD grown samples selected to highlight the chemical composition difference, namely samples #-1, #0, #1 and #2, where significant different morphologies are obtained. Indeed, while sample #-1 shows a planar morphology similar to that of positions #-2 and #-3, sample #0 exhibits a low density of MoS_2/MoO_2 microplates because of the high content of MoO_2, which is believed to have a significant effect on the planar morphology observed. The size of the MoS_2/MoO_2 microplates is in the 5-30 µm range for the sample #0. As we move towards the sample #1, the size of the MoS_2/MoO_2 microplates significantly decreases (1-3 µm range) and most interestingly the microplates are seen to pile up vertically as indicated by yellow arrows. This points up a clear morphological transition from planar to vertical MoS_2/MoO_2 nanosheets, accompanied with film densification. At the position #2, the MoS_2/MoO_2 nanosheets have completely disappeared with increasing of the MoS_2 content and giving place to the growth MoS_2 nanowires; another important morphological transformation. The vertical and the high aspect ratio of the MoS_2/MoO_2 nanostructures (whether nanosheets or nanowire bundles) of samples #1 and #2 along with their apparent inner open path could enhance their ability to absorb light and behave like “ideal” black bodies, as reflected from their very dark apparent color observed by optical microscopy.

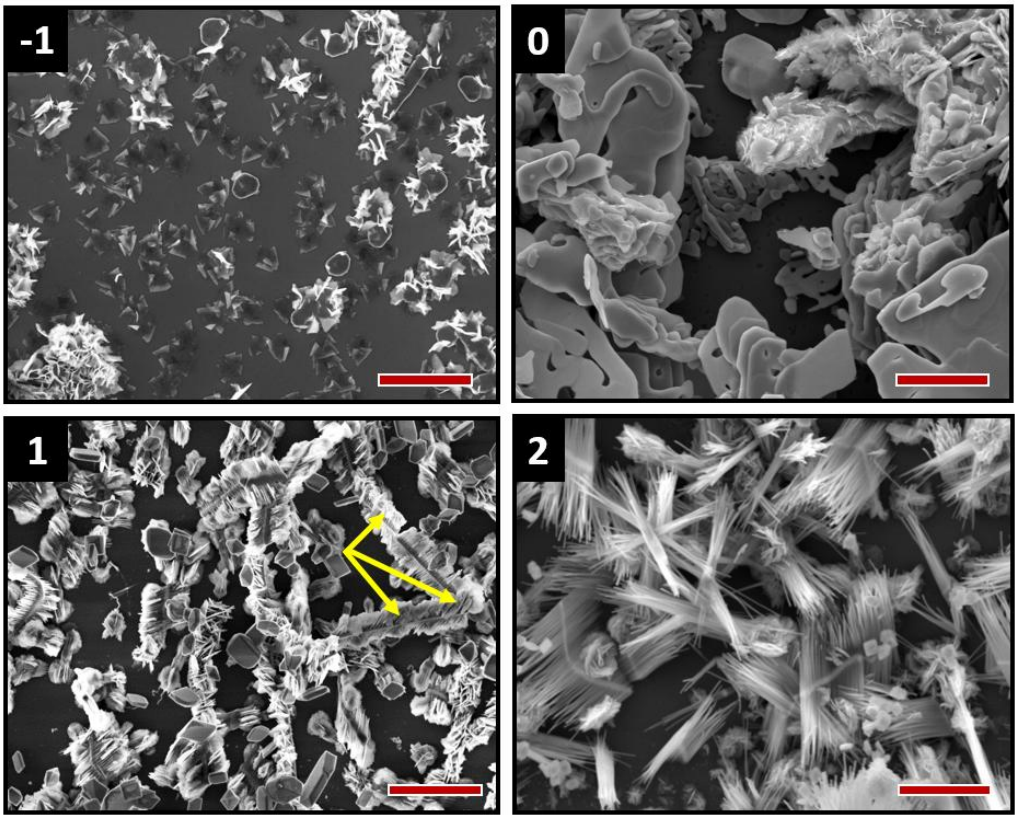

Figure 6. SEM images of the MoS_2/MoO_2 samples at the respective positions of #-1, #0, #1 and #2 in the CVD tube furnace (the scale bar for all images is 5 µm).

The HRTEM image of single-phase high-purity MoS_2 is presented in **Figure 7**a. The d-spacing of 2H-MoS_2 is displayed in the insert of **Figure 7**a and was found to be 0.62 nm, corresponding to the [002] plane. This confirms the high crystallinity of grown MoS_2, which supports further the above-discussed Raman and the XRD results. The **Figure 7**b, on the other hand, confirms the existence of nanograins consisting of the juxtaposition of 2H-MoS_2 and m-MoO2 lattices as confirmed by Raman spectroscopy. The d-spacing of the [110] planes of m-MoO_2 is 0.48 nm, as shown in the inset of **Figure 7**b, confirming again both the Raman and XRD results presented hereinbefore.

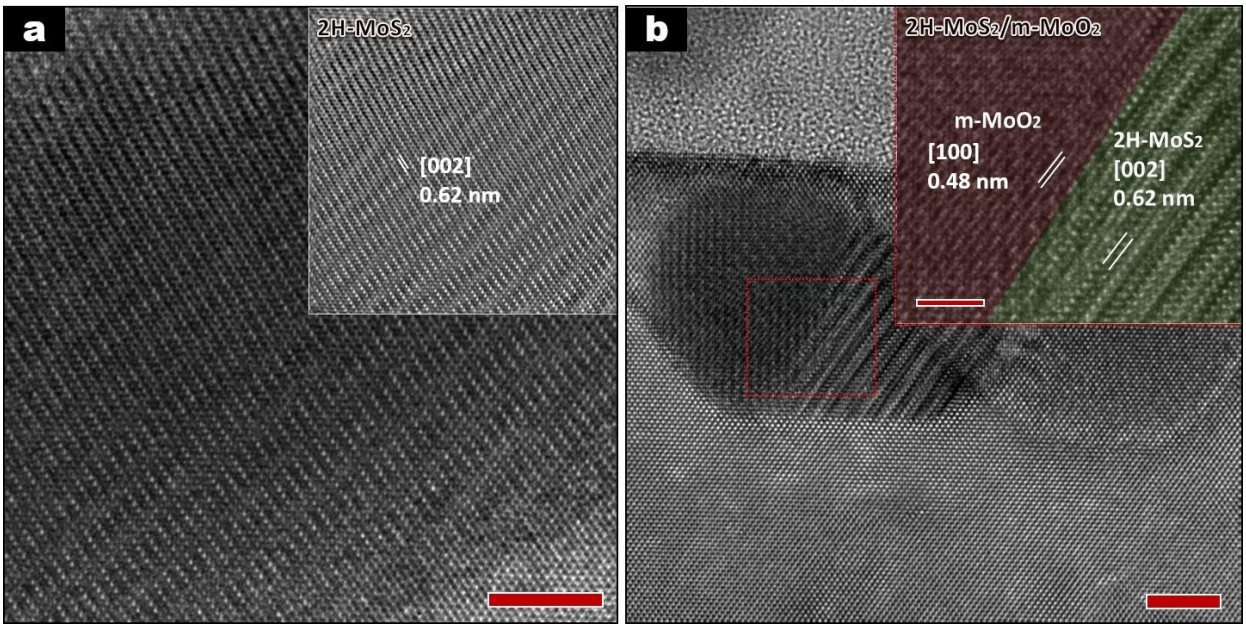

Figure 7. High-resolution TEM images of **a**. 2H-MoS_2 grain taken from sample #-3 and **b.** 2H-MoS_2/m-MoO_2 heterostructure from the sample positioned at #1. The scale bar here is 5 nm.

An interesting outcome from these HRTEM analyses, is the MoS_2/MoO_2 heterostructure nature which develops during the CVD growth. This indicates a good coherency between both lattices of MoS_2 and MoO_2 suggesting a combined macroscopic optical and electrical response. Indeed, the heterostructure could enhance many optical properties-based applications as its response to external light excitation will involve not only each material optical absorption but also it involves the new constructed heterostructure i.e., the combination of the two optical absorptions. In catalysis, this may trigger a Z-scheme reaction[47].

3.4. Optical properties

The reflectance spectra of the MoS_2/MoO_2 films samples are presented in **Figure 8**a. As can be seen, the MoS_2 samples #-2 and #-3 exhibit a reflectance that gradually decreases from ~35% to ~20% from UV towards the visible region and the excitons A and B are clearly visible at 636 and 688 nm positions, respectively[48]. The overall

recorded reflectance of all samples seems to follow a general trend in the full light range 350 nm up to 800nm consisting of a low light absorption for the sample #-3, followed by a gradual decrease to achieve the maximum light absorption for the sample #1, then a decrease of the light absorption towards the sample #4. One can notice the absence of the excitons A and B in heterostructure samples, provoked by the decrease of the content of planar MoS_2 and a concomitant increase in the MoO_2 content as seen in **Figure 8**b. It is clear that position #1 is offering the lowest reflectance for UV and most of the visible wavelengths. The reflectance spectra of **Fig. 8**a were also used to determine the optical bandgap of the MoS_2/MoO_2 films by using the Kubelka-Munk function[49]. Thus, the direct bandgaps of MoS_2/MoO_2 were deduced from the plot of $(F(R)h\nu)^2$ versus photon energy ($h\nu$), as illustratedin **Figure 8**c. The position dependence of the bandgap of the MoS_2/MoO_2 films is shown in **Figure 8**d. It is clearly seen that the bandgap of our MoS_2/MoO_2 heterostructure exhibits the maximum value of 2.4 eV for the sample #1 and a minimum value of 2 eV for the sample #2.

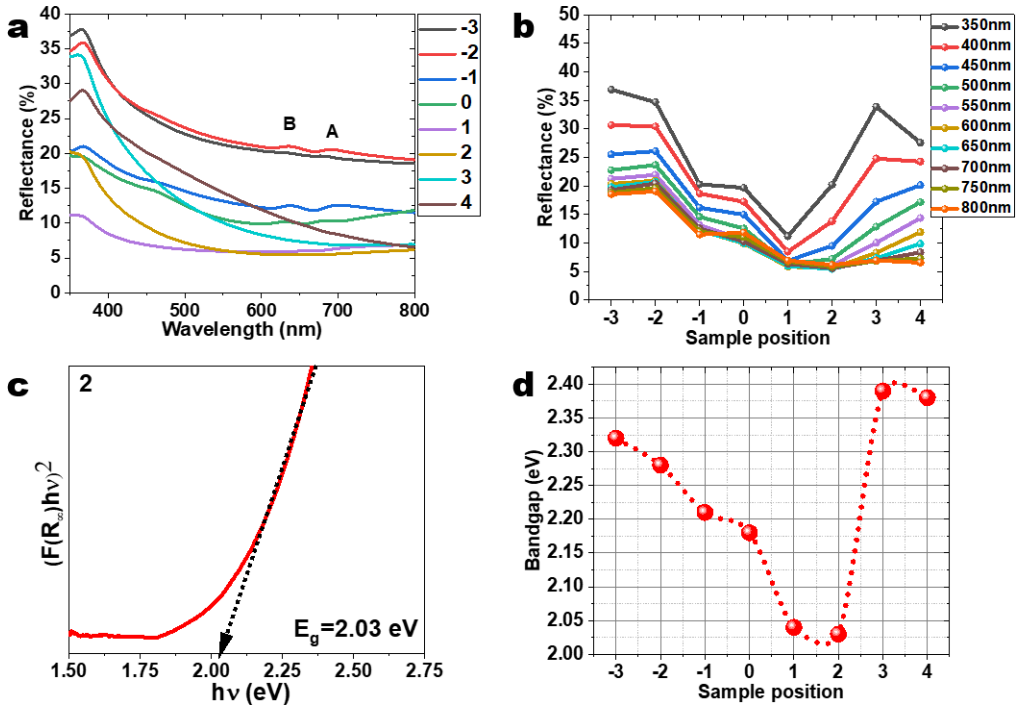

Figure 8. a. Reflectance spectra of the CVD grown MoS_2/MoO_2 samples at different positions; **b**. position dependence of the reflectance of the MoS_2/MoO_2 films for selected wavelengths; **c**. typical Tauc-plot of the Kubelka–Munk function for the determination of the direct bandgap of the sample #2; **d**. variation of the bandgap as function of the sample position.

The optical properties of samples #-2 and #2 were further characterized using spectroscopic ellipsometry and the result is depicted in **Figure 9**. The sample #-2 and #2 were selected for two main raisons: 1) these two samples are representative in term of the chemical composition of the all samples investigated, namely the sample #-2 represents the sole 2H-MoS_2 and the sample #2 the MoS_2/MoO_2 heterostructure, 2) both samples exhibit less pronounced roughness which avoid additional approximation to fit the optical ellipsometry spectroscopy results. For the sample #-2, we found several peaks in its ellipsometric spectrum. The presence of these peaks suggests a complex optical function for the thin film representing the convolution of several absorption peaks. In our model, we have considered four layers, namely the Si substrate, a thin interface layer of SiO_2 (2 nm), a dense layer of MoS_2 and a superficial rough layer (a mixture of MoS_2 and voids). The optical functions of silicon and SiO_2 are found in the database of the ellipsometer software. Then, we built the optical function of MoS_2 with the sum of eight Tauc-Lorentz oscillators as proposed in the work of Diware *et al.*[50]. After the fitting procedure, we found the following results concerning the structural properties of layers (see Table 1 in supplementary information). The **Figure 8**d&c summarize the fitting results of sample #-2, such as the refractive index and the extinction coefficient. This result is obtained for a thin film thickness of d_1= 10.5 nm; a roughness layer of d_2= 43 nm and a percentage of void in roughness 43.2 %. In addition, we can note that the optical function for MoS_2 found after the fitting procedure is in good agreement with the literature data[50]. In particular, we can note the presence of excitons A, B and C at 670 nm, 604 nm and 364 nm for the sample #-2 and not for the sample #2 as discussed in the optical properties section.

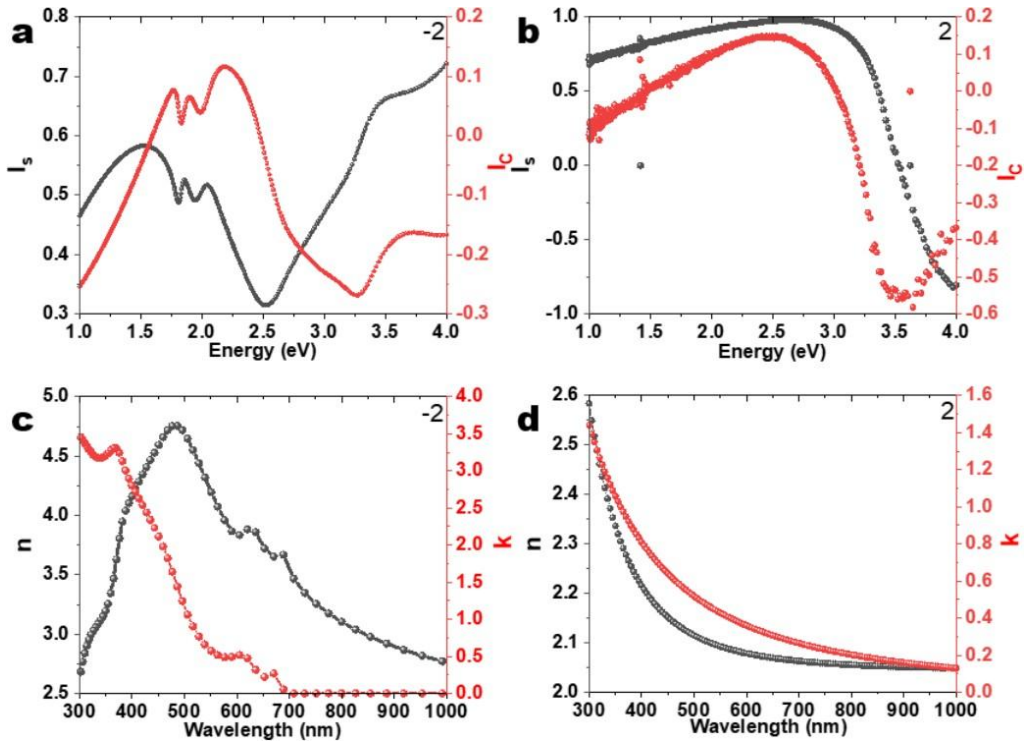

Figure 9. Ellipsometric I_s and I_c curves measured on sample #-2 **a.** and sample #2 **b**. and corresponding refractive indices and extinction coefficients from the ellipsometry spectroscopy, **c.** sample #-2 and **d**. sample #2.

For the sample #2, the ellipsometric spectrum is quite different from that of sample #-2, in the sense that it consists of only one oscillation. Consequently, we were not able to fit correctly the ellipsometric data as for sample #-2. We decided then to change the optical function of the thin film by a Cauchy absorbent function [51]. The best fit of the experimental data yielded the following results concerning the structural properties of layers: thin film thickness d_1= 51.3 nm; roughness layer d_2= 142 nm; percentage of void in roughness 89 %. Moreover, our values of the refractive index n = 2.08 at 632 nm were found to be slightly higher than those quoted in literature those for MoO_2 n=1.81 at 632 nm[52]. Such a small difference can be due to the presence of a little amount of MoS_2 in the thin film layer which can increases its effective refractive index.

3.5. Photoresponse measurements

To investigate the optoelectronic properties of the MoS_2/MoO_2 nanocomposite films, we sputter-deposited a pair of 50 nm thick Au electrodes at their surface (as illustrated in **Figure 10**a). Au was chosen because of its favorable

work function to minimize the contact barrier and improve the charge transport with MoS_2. The current density versus bias voltage (J–V) curves of our samples were acquired for all samples, at room temperature, under dark and illumination with a halogen lamp (70 mW/cm^2) as illustrated in **Figure10**b for the sample #2. The effective detection area of our samples was estimated (0.075 cm^2). For each sample, the photocurrent density defined by. ($J_{light} - J_{dark}$) is plotted as function of the applied voltage in **Figure 10**c.

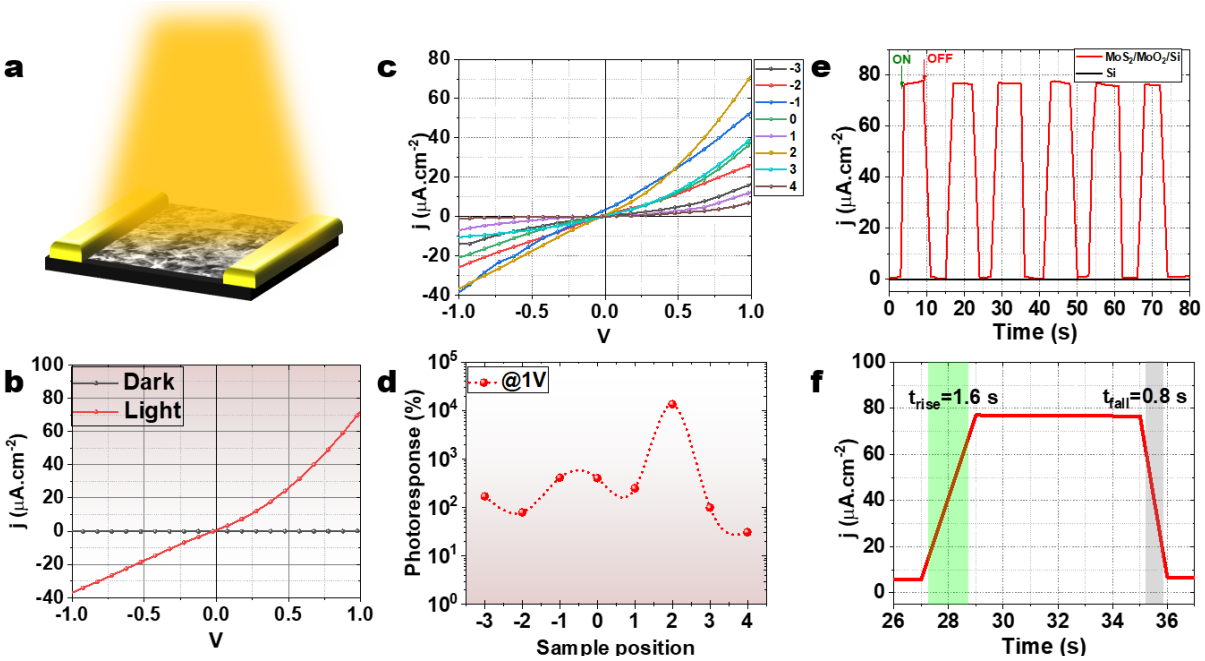

Figure 10. **a.** MoS_2/MoO_2 based photoconductive devices. **b.** typical J-V curve, here the result is from of the sample 2; **c.** photocurrent density curves of all samples; **d.** photoresponse dependence on sample position; **e.** transient photocurrent response of the sample #2 registered for six cycles ON/OFF every 10 s, under a constant halogen lamp illumination 70 mW.cm^{-2} and at applied bias of 1V; **f**. rise and decay times of the photoconductive device recorded for the sample #2.

As can be seen, the sample #2 is found to yield the highest photocurrent density of 70µA/cm^2 obtained at voltage bias of 1V. This high photogenerated current density recorded, is believed to result from its particular nanowires morphology. The nanowire shape appears to not only allow a strongly light absorption but it is also expected to provide a rapid charge transfer because of its one-dimensional structure. Subsequently, the photoresponce (P) at a biasing voltage of 1V was calculated using P(%) = 100 x [(I_{light}-I_{dark})/I_{dark}] and plotted for all samples in **Figure 10**d. It is evident that the sample grown at position #2 has again the highest photoresponse achieving 2.10^4 %, while the sample #4 has the lowest one of 30%. As aforementioned, such a high photoresponse is a

consequence of the very dense one-dimensional MoS_2 nanowires known for their ability to harvest light efficiently and ensure a rapid charge transfer[53–55]. Furthermore, we have calculated the responsivity (R) and the detectivity (D*) for the sample showing the best performances (position #2) at 1V using the following formula:

$$R = (\mathrm{I_{light}} - \mathrm{I_{dark}})/PS\ ;\ D^* = R/\sqrt{2\mathrm{qI_{dark}}}.$$

where P is the incident light's power density, S is the effective illuminated surface, and q is the absolute value of an electron charge (1.6 10^{19} Coulombs). For the sample #2, R and D* were found to be equal to 1.14 mA/W and 2.6 x 10^9 Jones, respectively. The obtained value of R is comparable to previous reported values [56,57]. It is worth to mention that other studies have reported high R values in the hundreds of A/W range obtained on very small surface area [17,58]. Note that our photoresponse result does not take into account the possible piezophototronic effect that could arise due to the MoS_2 interlayers strain as described elsewhere [56,57].

This work, we have mainly focused our attention on the investigation of the photoresponse of various generated microstructures that are simultaneously obtained with CVD while keeping relatively the same surface area. In this way, we can make the appropriate comparison while referring to the specific microstructure. Additional work is needed to examine the effect of excitation energies, active area, power density. Meanwhile, the high value of D* is comparable to other recently reported works[59–62]. Finally, **Figure 10**e shows the transient photocurrent response recorded at 1V bias of the MoS_2 based photoconductive device fabricated from the sample #2. The device is also exhibiting a relatively rapid time response as their typical rise and decay times defined as the time required to rise the photocurrent from 10% to 90% of its maximum value and vice versa- are found to be 1.6 s and 0.8 s, respectively, as depicted in **Figure 10**f. Such response times are comparable with the best values reported in literature for MoS_2[63–65].

Conclusion

In this work, the potential of the CVD approach to grow various MoS_2/MoO_2 nanocomposite structures has been demonstrated simply by changing the position of the substrates in the CVD furnace and controlling their proximity

to the precursors. Consequently, various structures, morphologies, compositions and optoelectronic properties were obtained. This work demonstrates the very rich playground offered by the CVD growth approach to develop pure MoS_2 to mixed phase MoS_2/MoO_2 heterostructure and explore their structural and optoelectronic properties. Our results have pointed out the position #2 to be the most appropriate zone to grow MoS_2/MoO_2 nanowires with high crystallinity and very interesting optoelectronic properties. Indeed, the integration of their integration into photoconductive devices enabled us to reveal their capacity to yield a photoresponse as high as 10^4-fold, a high responsivity of 1.13 mA/W, and specific detectivity of 2.6 x 10^9 Jones at an operating voltage as low as 1V. This suggests that further controlling the CVD growth of such structure is highly promising for the development of highly sensitive photodetectors in the full range of solar spectrum.

Acknowledgement: This work was performed in the context of a scientific collaboration between INRS and UPJV. D. Mouloua is grateful to both the Region HDF (France) and INRS (QC, Canada) for his PhD fellowship.

Financial support: Authors are thankful to financial support provided by the Natural Sciences and Engineering Research Council (NSERC) of Canada and Region of Haut-De-France.

Data availability statement: All data supporting this work are available upon request from the corresponding author: mustapha.jouiad@u-picardie.fr

Conflicts of Interest: The authors declare no conflict of interest

References

[1] W. Choi, N. Choudhary, G. H. Han, J. Park, D. Akinwande, Y. H. Lee, *Recent development of two-dimensional transition metal dichalcogenides and their applications*, Vol. 20, Elsevier B.V., **2017**, pp. 116–130.

[2] R. Mas-Ballesté, C. Gómez-Navarro, J. Gómez-Herrero, F. Zamora, *Nanoscale* **2011**, *3*, 20.

[3] A. Gupta, T. Sakthivel, S. Seal, *Prog. Mater. Sci.* **2015**, *73*, 44.

[4] T. Chowdhury, E. C. Sadler, T. J. Kempa, *Chem. Rev.* **2020**, *120*, 12563.

[5] Q. H. Wang, K. Kalantar-Zadeh, A. Kis, J. N. Coleman, M. S. Strano, *Nat. Nanotechnol.* **2012**, *7*, 699.

[6] A. Splendiani, L. Sun, Y. Zhang, T. Li, J. Kim, C. Y. Chim, G. Galli, F. Wang, *Nano Lett.* **2010**, *10*, 1271.

[7] J. Sun, X. Li, W. Guo, M. Zhao, X. Fan, Y. Dong, C. Xu, J. Deng, Y. Fu, *Crystals* **2017**, *7*, 1.

[8] D. Gupta, V. Chauhan, R. Kumar, *Inorg. Chem. Commun.* **2020**, *121*, 108200.

[9] N. Muhammad, Y. Chen, C. W. Qiu, G. P. Wang, *Nano Lett.* **2021**, *21*, 967.

[10] S. A. Svatek, E. Antolin, D. Y. Lin, R. Frisenda, C. Reuter, A. J. Molina-Mendoza, M. Muñoz, N. Agraït, T. S. Ko, D. P. De Lara, A. Castellanos-Gomez, *J. Mater. Chem. C* **2017**, *5*, 854.

[11] F. Guo, M. Li, H. Ren, X. Huang, W. Hou, C. Wang, W. Shi, C. Lu, *Appl. Surf. Sci.* **2019**, *491*, 88.

[12] S. Lin, X. Li, P. Wang, Z. Xu, S. Zhang, H. Zhong, Z. Wu, W. Xu, H. Chen, *Sci. Rep.* **2015**, *5*, 1.

[13] B. Su, H. He, Z. Ye, *Mater. Lett.* **2019**, *253*, 187.

[14] Z. Zhang, L. Huang, J. Zhang, F. Wang, Y. Xie, X. Shang, Y. Gu, H. Zhao, X. Wang, *Appl. Catal. B Environ.* **2018**, *233*, 112.

[15] Q. Li, N. Zhang, Y. Yang, G. Wang, D. H. L. Ng, *Langmuir* **2014**, *30*, 8965.

[16] A. Taffelli, S. Dirè, A. Quaranta, L. Pancheri, *Sensors* **2021**, *21*, 2758.

[17] H. S. Nalwa, *RSC Adv.* **2020**, *10*, 30529.

[18] H. Gao, C. Du, L. Chen, W. Wang, K. Li, *Adv. Mater. Interfaces* **2022**, *9*, 2102350.

[19] M. Peng, Y. Tao, X. Hong, Y. Liu, Z. Wen, X. Sun, *J. Mater. Chem. C* **2022**, *10*, 2236.

[20] A. Islam, J. Lee, P. X. L. Feng, *ACS Photonics* **2018**, *5*, 2693.

[21] G. Deokar, N. S. Rajput, P. Vancsó, F. Ravaux, M. Jouiad, D. Vignaud, F. Cecchet, J. F. Colomer, *Nanoscale* **2017**, *9*, 277.

[22] G. Deokar, P. Vancsó, R. Arenal, F. Ravaux, J. Casanova-Cháfer, E. Llobet, A. Makarova, D. Vyalikh, C. Struzzi, P. Lambin, M. Jouiad, J. F. Colomer, *Adv. Mater. Interfaces* **2017**, *4*, 1.

[23] G. Deokar, N. S. Rajput, J. Li, F. L. Deepak, W. Ou-Yang, N. Reckinger, C. Bittencourt, J. F. Colomer, M. Jouiad, *Beilstein J. Nanotechnol.* **2018**, *9*, 1686.

[24] I. S. Kim, V. K. Sangwan, D. Jariwala, J. D. Wood, S. Park, K. S. Chen, F. Shi, F. Ruiz-Zepeda, A. Ponce, M. Jose-Yacaman, V. P. Dravid, T. J. Marks, M. C. Hersam, L. J. Lauhon, *ACS Nano* **2014**, *8*, 10551.

[25] S. Wang, Y. Rong, Y. Fan, M. Pacios, H. Bhaskaran, K. He, J. H. Warner, *Chem. Mater.* **2014**, *26*, 6371.

[26] J. Jeon, S. K. Jang, S. M. Jeon, G. Yoo, Y. H. Jang, J. H. Park, S. Lee, *Nanoscale* **2015**, *7*, 1688.

[27] T. Nam Trung, F. Z. Kamand, T. M. Al tahtamouni, *Appl. Surf. Sci.* **2020**, *505*.

[28] J. Chen, W. Tang, B. Tian, B. Liu, X. Zhao, Y. Liu, T. Ren, W. Liu, D. Geng, H. Y. Jeong, H. S. Shin, W. Zhou, K. P. Loh, *Adv. Sci.* **2016**, *3*, 3.

[29] H. F. Liu, S. L. Wong, D. Z. Chi, *Chem. Vap. Depos.* **2015**, *21*, 241.

[30] D. Mouloua, A. Kotbi, G. Deokar, K. Kaja, M. El Marssi, M. Ali, E. L. Khakani, M. Jouiad, *Materials (Basel).* **2021**, *14*, 3283.

[31] C. M. Hyun, J. H. Choi, S. W. Lee, J. H. Park, K. T. Lee, J. H. Ahn, *J. Alloys Compd.* **2018**, *765*, 380.

[32] Z. Yin, X. Zhang, Y. Cai, J. Chen, J. I. Wong, Y. Y. Tay, J. Chai, J. Wu, Z. Zeng, B. Zheng, H. Y. Yang, H. Zhang, *Angew. Chemie - Int. Ed.* **2014**, *53*, 12560.

[33] T. Chiawchan, H. Ramamoorthy, K. Buapan, R. Somphonsane, *Nanomaterials* **2021**, *11*, 2642.

[34] J. V. Pondick, J. M. Woods, J. Xing, Y. Zhou, J. J. Cha, *ACS Appl. Nano Mater.* **2018**, *1*, 5655.

[35] P. Wang, J. Lei, J. Qu, S. Cao, H. Jiang, M. He, H. Shi, X. Sun, B. Gao, W. Liu, *Chem. Mater.* **2019**, *31*, 873.

[36] J. Yan, A. Rath, H. Wang, S. H. Yu, S. J. Pennycook, D. H. C. Chua, *Mater. Res. Lett.* **2019**, *7*, 275.

[37] Y. Huang, J. Guo, Y. Kang, Y. Ai, C. M. Li, *Nanoscale* **2015**, *7*, 19358.

[38] L. K. Tan, B. Liu, J. H. Teng, S. Guo, H. Y. Low, K. P. Loh, *Nanoscale* **2014**, *6*, 10584.

[39] G. Pradhan, A. K. Sharma, *Mater. Res. Bull.* **2018**, *102*, 406.

[40] S. Erfanifam, S. M. Mohseni, L. Jamilpanah, M. Mohammadbeigi, P. Sangpour, S. A. Hosseini, A. Iraji Zad, *Mater. Des.* **2017**, *122*, 220.

[41] S. Kang, Y. S. Kim, J. H. Jeong, J. Kwon, J. H. Kim, Y. Jung, J. C. Kim, B. Kim, S. H. Bae, P. Y. Huang, J. C. Hone, H. Y. Jeong, J. W. Park, C. H. Lee, G. H. Lee, *ACS Appl. Mater. Interfaces* **2021**, *13*, 1245.

[42] R. I. Romanov, A. S. Slavich, M. G. Kozodaev, D. I. Myakota, Y. Y. Lebedinskii, S. M. Novikov, A. M. Markeev, *Phys. Status Solidi - Rapid Res. Lett.* **2020**, *14*, 1.

[43] R. D. Nikam, A. Y. Lu, P. A. Sonawane, U. R. Kumar, K. Yadav, L. J. Li, Y. T. Chen, *ACS Appl. Mater. Interfaces* **2015**, *7*, 23328.

[44] X. Jiang, M. Fuji, *Catal. Letters* **2021**, 1.

[45] N. Iqbal, I. Khan, A. Ali, A. Qurashi, *J. Adv. Res.* **2022**, *36*, 15.

[46] H. Nan, Z. Wang, W. Wang, Z. Liang, Y. Lu, Q. Chen, D. He, P. Tan, F. Miao, X. Wang, J. Wang, Z. Ni, *ACS Nano* **2014**, *8*, 5738.

[47] J. Abed, N. S. Rajput, A. El Moutaouakil, M. Jouiad, *Nanomaterials* **2020**, *10*, 1.

[48] B. Mukherjee, F. Tseng, D. Gunlycke, K. K. Amara, G. Eda, E. Simsek, *Opt. Mater. Express* **2015**, *5*, 447.

[49] X. Fan, P. Xu, D. Zhou, Y. Sun, Y. C. Li, M. A. T. Nguyen, M. Terrones, T. E. Mallouk, *Nano Lett.* **2015**, *15*, 5956.

[50] M. S. Diware, K. Park, J. Mun, H. G. Park, W. Chegal, Y. J. Cho, H. M. Cho, J. Park, H. Kim, S. W. Kang, Y. D. Kim, *Curr. Appl. Phys.* **2017**, *17*, 1329.

[51] A. R. Frias, M. A. Cardoso, A. R. N. Bastos, S. F. H. Correia, P. S. André, L. D. Carlos, V. de Z. Bermudez, R. A. S. Ferreira, *Energies* **2019**, *12*.

[52] O. De Melo, V. Torres-Costa, A. Climent-Font, P. Galán, A. Ruediger, M. Sánchez, C. Calvo-Mola, G. Santana, V. Torres-Costa, *J. Phys. Condens. Matter* **2019**, *31*.

[53] H. Liao, Y. Wang, S. Zhang, Y. Qian, *Chem. Mater.* **2001**, *13*, 6.

[54] C. Yu, H. Xu, Y. Sun, X. Zhao, Z. Hui, Y. Gong, R. Chen, Q. Chen, J. Zhou, G. Sun, W. Huang, *Carbon N. Y.* **2020**, *170*, 543.

[55] M. Liu, K. Hisama, Y. Zheng, M. Maruyama, S. Seo, A. Anisimov, T. Inoue, E. I. Kauppinen, S. Okada, S. Chiashi, R. Xiang, S. Maruyama, *ACS Nano* **2021**, *15*, 8418.

[56] M. Javadi, S. Darbari, Y. Abdi, F. Ghasemi, *IEEE Electron Device Lett.* **2016**, *37*, 677.

[57] P. T. Gomathi, P. Sahatiya, S. Badhulika, *Adv. Funct. Mater.* **2017**, *27*, 1701611.

[58] R. Ghalamboland, S. Darbari, M. Rashidifar, Y. Abdi, *IEEE Sens. J.* **2021**, *21*, 14784.

[59] A. Xie, Y. Jian, Z. Cheng, Y. Gu, Z. Chen, X. Song, Z. Yang, *J. Phys. Condens. Matter* **2022**, *34*.

[60] Y. Yin, Y. Guo, D. Liu, C. Miao, F. Liu, X. Zhuang, Y. Tan, F. Chen, Z. xing Yang, *Adv. Opt. Mater.* **2022**, *10*, 1.

[61] D. Liu, F. Liu, Y. Liu, Z. Pang, X. Zhuang, Y. Yin, S. Dong, L. He, Y. Tan, L. Liao, F. Chen, Z. xing Yang, *Small* **2022**, *18*, 1.

[62] X. Liu, J. Luo, Y. Lin, Z. Lin, X. Liu, J. He, W. Yu, Q. Liu, T. Wei, J. Yang, W. Zhang, J. Guo, *ACS Appl. Electron. Mater.* **2021**, *3*, 5415.

[63] Y. Wu, Z. Li, K.-W. Ang, Y. Jia, Z. Shi, Z. Huang, W. Yu, X. Sun, X. Liu, D. Li, *Photonics Res.* **2019**, *7*, 1127.

[64] A. E. Yore, K. K. H. Smithe, S. Jha, K. Ray, E. Pop, A. K. M. Newaz, *Appl. Phys. Lett.* **2017**, *111*, 043110.

[65] B. Sun, Z. Wang, Z. Liu, X. Tan, X. Liu, T. Shi, J. Zhou, G. Liao, *Adv. Funct. Mater.* **2019**, *29*, 1.